THE JOURNAL OF PHYSICAL CHEMISTRY C
A JOURNAL OF THE AMERICAN CHEMICAL SOCIETY

pubs.acs.org/JPCC

Article

Assessing Diffusion Relaxation of Interlayer Water in Clay Minerals Using a Minimalist Three-Parameter Model

Martin H. Petersen, Nathan Vernet, Will P. Gates, Félix J. Villacorta, Seiko Ohira-Kawamura, Yukinobu Kawakita, Masatoshi Arai, Gerald Kneller,* and Heloisa N. Bordallo*

Cite This: https://doi.org/10.1021/acs.jpcc.1c04322

Read Online

ACCESS | Metrics & More | Article Recommendations | Supporting Information

ABSTRACT: Using a minimal model approach for interpreting the intermediate scattering function, $F(\mathbf{Q}, t)$, to analyze quasi-elastic neutron scattering (QENS) data from interlayer water as a function of temperature in the 2D-layered clay minerals montmorillonite (Mt) and hectorite (Ht) a clear difference in behavior was observed. This was related to the polarization effect induced on the water molecules by both the exchangeable cation and surface charge within the interlayer. Although crucial for improving the wide range of industrial applications of clays as well as for explaining water uptake and retention by clays such information is neither obtained straightforwardly by other experimental methods nor fully accounted by molecular dynamics simulations. Furthermore, analysis of the evolution of the fitted parameters as a function of temperature shows that hydrogen atoms have a relaxation with a smaller average motional amplitude for Mt. Physically this can be explained as stronger hydrogen-bonding by water at the interlayer surfaces in Mt. These results allow for a novel and realistic description of these nanomaterials at the atomic scale, which is crucial for improving functional properties. These findings also prove that this new approach to modeling QENS captures subtle changes hidden in the spectra.

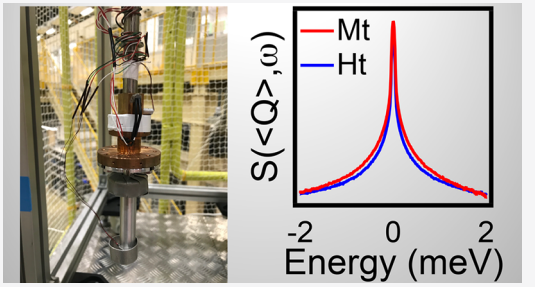

INTRODUCTION

Expandable smectite clays are among the most abundant naturally occurring nanomaterials on Earth. These soft, layered materials are formed by SiO_4 tetrahedra on either side of a sheet of Al- or Mg-octahedra, resulting in stacked unit layers separated by an interlayer space. All smectites have some degree of isomorphous substitution by a cation of lower valence in either of the unit layers. This results in a net negative charge of the layers that is compensated by hydrated and exchangeable interlayer cations, i.e., cations which do not belong to the crystalline structure, but instead reside within the interlayer. The surface charge and charge-balancing interlayer cations enable clay minerals to swell during uptake of water and are key to many applications including water treatment, bioactive molecule intercalation (drug delivery), soil remediation, and CO_2 capture as well as extraterrestrial environment studies.[1−7]

Water is by far the most important adsorbed molecule in the interlayer space, where it interacts with the exchangeable cations and the siloxane surface. In the interlayer region the surface negative charge is partially compensated by the charge of the cation. This implies that both surface and cation charge−dipole attraction are the origins of clay−water interactions and control water mobility within this nanoconfined region of expandable minerals. Mobility of confined water molecules within the interlayer underpins most of the functional properties of these nanomaterials.[8,9] However, how the properties of H_2O are influenced by their close proximity to the clay-mineral surface itself is still not fully understood, and direct information on the polarization effect on the water molecules dynamics is still missing.[10−13] To gain further insight on this question, we used quasi-elastic neutron scattering (QENS) to explore the influence of layer charge resulting from isomorphic substitution within the octahedral sheet of two different types of smectite (dioctahedral Mt and trioctahedral Ht) on diffusion of interlayer water as a function of temperature. To this end, two sodium smectite clay minerals, having the same hydration level, with one water layer in the interlayer space, where Na^+ is surrounded by 3−3.5 water molecules, were selected for this work, a montmorillonite ($Na_{0.82}Mg_{0.72}Fe_{0.4}Si_{7.9}Al_{2.98}O_{20}(OH)_4$, with a layer charge equal to 0.82 e^-/unit cell, hereafter Mt) and a hectorite ($Na_{0.68}Mg_{5.42}Li_{0.58}Si_{7.9}Al_{0.1}O_{20}(OH)_4$, with a layer charge equal to 0.68 e^-/unit cell, hereafter Ht). The larger net negative charge of the Mt layers stems from the fact that two of its three octahedral sites are occupied predominantly by trivalent cations (Al^{3+}) with partial isomorphic substitution of

Received: May 15, 2021
Revised: June 22, 2021

Mg^{2+} as well as partial substitution of Al^{3+} for Si^{4+} in the tetrahedral sheet. On the other hand, for Ht, all three octahedral sites are occupied predominantly by divalent cations (e.g., Mg^{2+}) with some isomorphic substitution of Li^{+}, but nil substitution in the tetrahedral sheet.[14,15]

QENS is an ideal tool for the study of confined water due to the extraordinarily high incoherent scattering cross-section of the hydrogen atoms, allowing study of the self-diffusion of water, i.e., how the average position of these scattering centers autocorrelate in time, from 10^{-9} to 10^{-13} s, and space, from 1 to 100 Å.[6,16] Such information is vital for poorly ordered heterogeneous materials such as clay minerals, because competing short- and long-range interactions result in frustration, while complex coupling between different variables leads to non-Markovian, scale-invariant multiple relaxation processes.[8,17,18] In QENS experiments these variables are the positions of the H atoms in time. In sharp contrast to currently used classical diffusion models, which work well only for simulating simple processes, here we demonstrate that the proposed new minimalistic energy landscape-based method for QENS analysis can accurately describe such multiscale atomic motions, which has so far been used to describe internal protein dynamics.[19,20] The underlying idea is, in fact, a quantum mechanical energy landscape-based theory of neutron scattering,[21] which has much in common with the Franck–Condon theory of molecular spectroscopy,[22] on which QENS models for complex systems can be built.

In the present article, using this new framework, the fitted parameters are directly related to the energetics of the clay–water system and described as a series of overlapping potential energy wells with many local minima and a distribution of barrier heights localized within a restricted domain of phase space. Within the (semi)classical interpretation of the energy landscape concept, the momentum transfer, $\mathbf{Q}$, defines a spatial resolution of the motions in the sample on an essentially fractal manner. Thus, this analysis leads to a realistic kinetic picture for the motional heterogeneity of the diffusing water molecules, noting that with decreasing Q, diffusive motions with different time scales contribute to the observed dynamics. The tracking of the changes in the QENS spectra as a function of temperature was used to follow how the confined water molecules in the interlayer of the clays behaved in the so-called supercooled state.[17]

MINIMAL MODEL FOR QENS DATA

The quantity of interest from QENS experiments is the dynamic structure factor, $S(\mathbf{Q}, \omega)$, which describes the microscopic dynamics of a scattering system and is related to the double differential scattering cross-section via[23]

$$\frac{d^2\sigma}{d\Omega d\omega} = \frac{k_f}{k_i} S(\mathbf{Q}, \omega) \tag{1}$$

where k_i and k_f are the initial and final length of the neutron wave vector, respectively, and $\mathbf{Q}$ and ω are, respectively the momentum and energy transfer from the neutron to the sample. The dynamic structure factor can be expressed as

$$S(\mathbf{Q}, \omega) = \frac{1}{2\pi}\int_{-\infty}^{\infty} dt e^{-i\omega t} F(\mathbf{Q}, t) \tag{2}$$

where $F(\mathbf{Q}, t)$ is the intermediate scattering function. In hydrated Mt and Ht, incoherent scattering from the hydrogen atoms dominates the measured signal and the double differential scattering cross-section is approximately given by

$$F(\mathbf{Q}, t) \approx F_s(\mathbf{Q}, t) = \frac{|b_{H,inc}|^2}{N_H} \sum_j \langle e^{-i\mathbf{Q}\cdot\mathbf{r}_j(0)} e^{i\mathbf{Q}\cdot\mathbf{r}_j(t)} \rangle \tag{3}$$

where N_H is the number of scattered hydrogen atoms, $\mathbf{r}_j(t)$ is the position operator of the jth hydrogen atom, and $F(\mathbf{Q}, t)$ is the total intermediate scattering function. Because incoherent scattering probes only self-correlations of the atomic motions, we use the notation $F_s(\mathbf{Q}, t)$ for the dominant component due to incoherent scattering from hydrogen.

It follows from the symmetry properties of the quantum time correlation functions that $F(\mathbf{Q}, t)$ and $S(\mathbf{Q}, \omega)$ fulfill the detailed balance relation,

$$F(\mathbf{Q}, t) = F(-\mathbf{Q}, -t + i\beta\hbar) \tag{4}$$

$$S(\mathbf{Q}, \omega) = S(-\mathbf{Q}, -\omega) e^{\beta\hbar\omega} \tag{5}$$

where $\beta = 1/k_B T$, k_B is the Boltzmann constant, and T is the temperature in Kelvin.

Because the water in the samples are confined, the motional amplitudes of individual hydrogen atoms are considered finite and intermediate scattering function tends to a finite plateau value,

$$\lim_{t\to\infty} F(\mathbf{Q}, t) = \sum_j |\langle e^{i\mathbf{Q}\cdot\mathbf{r}_j} \rangle|^2 = \mathrm{EISF}(\mathbf{Q}) \tag{6}$$

where EISF stands for elastic incoherent structure factor. Defining

$$\delta\hat{\rho}_j(\mathbf{Q}, t) = e^{i\mathbf{Q}\cdot\mathbf{r}_j(t)} - \langle e^{i\mathbf{Q}\cdot\mathbf{r}_j} \rangle = \hat{\rho}_j(\mathbf{Q}, t) - \langle \hat{\rho}_j(\mathbf{Q}) \rangle$$

to be the deviation of the spatially Fourier transformed single particle density of atom j, $\hat{\rho}_j(\mathbf{Q}, t)$, with respect to its mean value, the intermediate scattering function can be written in the generic form[19,20]

$$F(\mathbf{Q}, t) = \mathrm{EISF}(\mathbf{Q}) + (1 - \mathrm{EISF}(\mathbf{Q}))\phi(\mathbf{Q}, t) \tag{7}$$

where the relaxation function, $\phi(\mathbf{Q}, t)$, is given by

$$\phi(\mathbf{Q}, t) = \frac{\sum_j \langle \delta\hat{\rho}_j^{\dagger}(\mathbf{Q}, 0)\delta\hat{\rho}_j(\mathbf{Q}, t) \rangle}{\sum_j \langle \delta\hat{\rho}_j^{\dagger}(\mathbf{Q}, 0)\delta\hat{\rho}_j(\mathbf{Q}, 0) \rangle} \tag{8}$$

This function is normalized such that $\phi(\mathbf{Q}, 0) = 1$ and relaxes to zero as t tends to infinity, $\lim_{t\to\infty}\phi(\mathbf{Q}, t) = 0$. Being a quantum time correlation function, it fulfills moreover the detailed balance relation

$$\phi(\mathbf{Q}, t) = \phi(-\mathbf{Q}, -t + i\beta\hbar) \tag{9}$$

For the further analysis, we introduce the symmetrized version,[19,20]

$$\phi^{(+)}(\mathbf{Q}, t) = \frac{\phi(\mathbf{Q}, t + i\beta\hbar/2)}{\phi(\mathbf{Q}, i\beta\hbar/2)} \tag{10}$$

which is real and symmetric in time, as its classical counterpart, and we use the semiclassical approximation[24]

$$\phi^{(+)}(\mathbf{Q}, t) \approx \phi^{(cl)}(\mathbf{Q}, t) \tag{11}$$

By construction, the normalization condition $\phi^{(+)}(\mathbf{Q}, 0) = 1$, and we use this function to define the corresponding normalized and symmetrized intermediate scattering function

https://doi.org/10.1021/acs.jpcc.1c04322
J. Phys. Chem. C XXXX, XXX, XXX−XXX

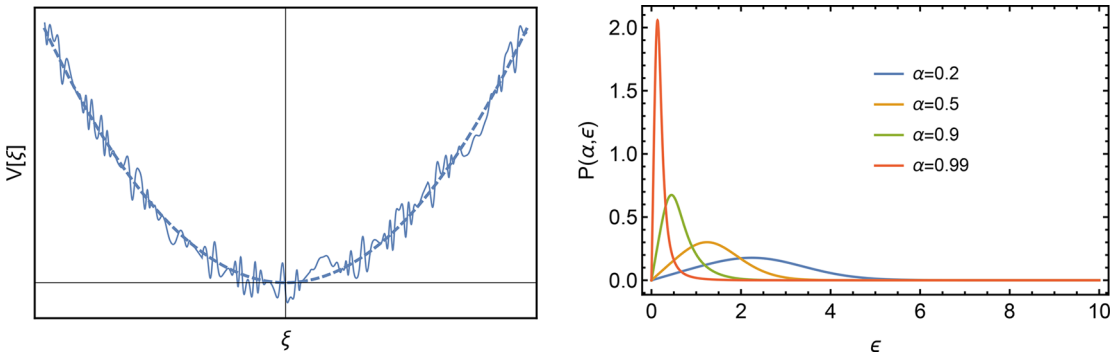

Figure 1. Left panel: Sketch of a "rough" harmonic potential with many minima. The dashed line is the smooth version of the potential corresponding to $\alpha = 1$. Right panel: Distribution of the dimensionless energy barrier heights for various values of α. For $\alpha \to 1$, the center of the distribution is located close to $\epsilon = 0$.

$$F^{(+)}(\mathbf{Q}, t) = \mathrm{EISF}(\mathbf{Q}) + (1 - \mathrm{EISF}(\mathbf{Q}))\phi^{(+)}(\mathbf{Q}, t) \tag{12}$$

The above expression will be used for the analysis of QENS data to be described in the following.

To account for self-similar relaxation dynamics of the hydrogen atoms, we represent the relaxation function by a "stretched" Mittag−Leffler function,[19−21]

$$\phi^{(+)}(t) = E_\alpha(-(t/\tau)^\alpha) \quad (0 < \alpha \leq 1, \tau > 0) \tag{13}$$

where α determines the form and τ sets the time scale. The Mittag−Leffler function $E_\alpha(z)$ is an entire function in the complex plane which is defined by the Taylor series,[25]

$$E_\alpha(z) = \sum_{k=0}^{\infty} \frac{z^k}{\Gamma(1 + k\alpha)} \tag{14}$$

and can be considered as a generalization of the exponential function, which is retrieved for $\alpha = 1$, because $\Gamma(1 + k) = k!$ and therefore

$$E_1(z) = \sum_{k=0}^{\infty} \frac{z^k}{k!} = \exp(z)$$

where $\Gamma(z)$ is the gamma function or generalized factorial. We note that $\lim_{\alpha\to 0} E_\alpha(z) = 1/2$ for any $t > 0$. The asymptotic form of the stretched Mittag−Leffler function is given by

$$E_\alpha(-(t/\tau)^\alpha)t \underset{\sim}{\gg} \tau\frac{(t/\tau)^{-\alpha}}{\Gamma(1 - \alpha)} \tag{15}$$

and because $\lim_{\alpha\to 1} 1/\Gamma(1 - \alpha) = 0$, the long time tail in eq 15 will vanish for exponential relaxation.

Furthermore, relaxation functions of the form of eq 13 can be derived from the fractional Ornstein−Uhlenbeck process, which includes the non-Markovian memory effect resulting from Brownian particle interactions with other particles in its environment.[26] The dynamical variable is here not the position of a diffusing Brownian particle but the deviation of the Fourier transformed particle density with respect to its mean value,[19,20]

$$\xi(\mathbf{Q}, t) = \exp(i\mathbf{Q}\cdot\mathbf{r}(t)) - \langle\exp(i\mathbf{Q}\cdot\mathbf{r})\rangle \tag{16}$$

The nonexponential form of the relaxation function eq 13 can be seen as the result of a diffusion in a "rough" harmonic potential (see left panel of Figure 1), which "traps" the dynamical variable in a local minimum and where the roughness is defined by a distribution of dimensionless energy barriers separating the local minima,[19,20]

$$P(\alpha, \epsilon) = \frac{2\epsilon \sin(\pi\alpha)}{\pi(e^{\alpha\epsilon^2} + e^{-\alpha\epsilon^2} + 2\cos(\pi\alpha))} \tag{17}$$

where ϵ is defined through

$$\epsilon = \frac{\Delta E}{k_B T} \tag{18}$$

with ΔE being the physical energy barrier height. The right panel of Figure 1 shows the energy barrier distribution for different values of α. Here smaller values of α lead to a "rough" harmonic potential, with a wide distribution energy barriers, including very large ones, but for $\alpha = 1$, we have a smooth harmonic potential with $\Delta E = 0$.

EXPERIMENTAL DETAILS

Quasi-elastic Neutron Scattering Data Collection and Data Analysis Strategy. QENS data were obtained using the AMATERAS spectrometer installed at the Spallation Neutron Source at the Materials and Life Science Experimental Facility (MLF) of J-PARC, Japan. AMATERAS is a cold, direct geometry time-of-flight spectrometer (ToF).[27] Data were collected using an incident beam of neutrons with $\lambda = 5.2$ Å, corresponding to $E_i = 3$ meV and $\Delta E = 54$ μeV. Samples were mounted in cylindrical sample holders, and measurements were conducted for Mt and Ht between 150 and 300 K. Vanadium was used to determine the instrument resolution, and the background was obtained by measuring an empty sample holder at 300 K. Using the UTSUSEMI reduction program available at J-PARC,[28] the instrumental background was subtracted and the data were transformed into the dynamic structure factor of the form $S(Q, \omega)$, with $|\mathbf{Q}| = Q$ defined as the magnitude of the scattering vector and ω the energy transfer. The spectra were grouped to obtain seven constant scattering vectors in the range 0.4 Å^{-1} ≤ Q ≤ 1.6 Å^{-1} with an equal spacing of 0.2 Å^{-1}. The uncertainties for $S(Q, \omega)$ were estimated based on Poisson statistics.

Before using the proposed approach, we must consider the instrumental resolution, which in the experimentally observed dynamic structure factor is given by a convolution:[29]

$$S_R(\mathbf{Q}, \omega) = (S^*\tilde{R})(\mathbf{Q}, \omega) = \int_{-\infty}^{\infty} d\omega' S(\mathbf{Q}, \omega - \omega')\tilde{R}(\mathbf{Q}, \omega') \tag{19}$$

where $\tilde{R}(\mathbf{Q}, \omega)$ represents the Q-dependent instrumental resolution function, which is obtained by a vanadium run,

https://doi.org/10.1021/acs.jpcc.1c04322
J. Phys. Chem. C XXXX, XXX, XXX−XXX

and the index "R" represents a "resolution-broadened" function.[20] To eliminate the resolution-broadening and thereby obtain a deconvolved spectra, an inverse Fourier transformation was performed and the convolution theorem $F_R(Q, t) = F(Q, t)R(Q, t)$ applied.[29] This implies that with the proposed minimal model approach for analyzing QENS data, the following apply:

(i) The deconvolved and symmetrized $F^{(+)}(Q, t)$ can be fitted the simple model described by eq 12.

(ii) The parameters obtained by analyzing the intermediate scattering function using the stretched Mittag−Leffler function as the relaxation function, are the EISF(Q), the form parameter $\alpha(Q)$ and the time scale parameter $\tau(Q)$. Note that here EISF(Q) describes the average motional amplitude of the atomic motion, while the parameters $\tau(Q)$ and $\alpha(Q)$ describe their relaxation dynamics, i.e., $\tau(Q)$ describes the time scale of the relaxation probed within the instrumental time scale and $\alpha(Q)$ the form of the relaxation. A decrease in $\tau(Q)$ means faster relaxation, whereas $\alpha(Q) = 1$ indicates an exponential form of the relaxation and thus a diffusion in a normal harmonic potential.

(iii) Even if our experimental data were reduced with a good estimate of the error bars, we have refrained from including the statistical error bars in the F(Q,t) spectra because the numerical Fourier transform might produce aliasing errors,[20] a well-known issue in many other experimental techniques.[30,31] This implies that to apply this model as a transformative tool to analyze QENS data, further work on other statistical methods is needed to estimate the uncertainties for the $F(Q, t)$ through the Fourier transformation.

Analysis of the $F(Q, t)$ data for Mt and Ht was carried out in Python using eq 12 and eq 13 to describe the relaxation processes. For data evaluation, differently from the normal $S(Q, \omega)$ QENS analysis, where model fitting is performed by a χ^2 minimization procedure using the Levenberg−Marquardt algorithm to perform a least-square fit,[32] we have used Iminuit, a Jupyter-friendly Python interface for the Minuit2 C++ library maintained by CERN's ROOT team.[33] This minimization method is most commonly used for likelihood fits of models to data. In other words, Minuit2 is a tool to find the minimum value of a multiparameter function (the "FCN") and to analyze the shape of the function around the minimum. Thus, Minuit is usually used to find the "best" values of a set of parameters, where "best" is defined as those values which minimize a given function. As in the common case of a least-squares fit, FCN is defined as a χ^2, and we sought to minimize this value for each fit.

To circumvent the shortcoming mentioned in iii, the reconstructed experimental $S(Q, \omega)$ spectra, obtained using the parameters obtained from the fits in time domain, plotted together with the residuals (see Supporting Information), showed an equal distribution of the residuals around zero, with no systematic trends and a considerably good and defensible χ^2 for all Q-values.[31]

Thermal Analysis Data Collection. The mass loss and energetics of the water in the samples were quantified by thermal gravimetric analysis (TGA) and differential scanning calorimetry (DSC) measurements using, respectively, a TG 209F1 LIBRA and a DSC 214 Polyma from NETZSCH. The experimental conditions were N_2 atmosphere ≈ (40 mL/min), heating rate (10 K/min), platinum top-opened crucible (TGA), and aluminum closed crucible (DSC). The sample weights were approximately 20 mg. The results allowed us to quantify the amount of initial H_2O in the clay mineral layers as well as to obtain the enthalpy of the evaporation.

RESULTS AND DISCUSSION

Figure 2 shows the DSC curves for Ht and Mt on heating up to 200 °C. In the case of Mt, a transition is observed at 151 °C

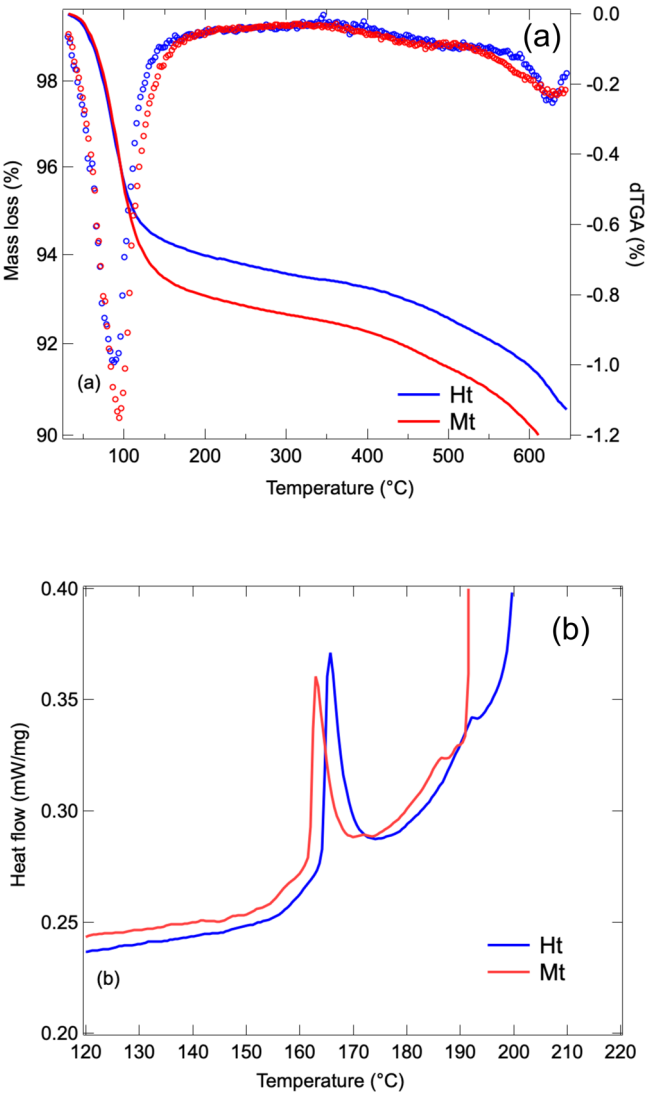

Figure 2. Thermogravimetric analysis for Mt and Ht plotted as a function of temperature. (a) Results from the TGA are expressed as percentage mass. Mass loss (solid lines) refers to the left *y*-axis, while its derivative (dTGA) to the right *y*-axis (open dots). (b) Calorimetry (DSC) data are expressed as enthalpy change in mW per mg.

(with an associated enthalpy, ΔH, of 212 J/g), while for Ht this transition is observed at lower temperature, i.e., 138 °C (ΔH = 202 J/g). These endothermic transitions, Figure 2(b), are related to the cessation of water loss from the interlayer observed in the TGA data. For Ht, we observed a first peak on the dTGA, defined as the negative of the differential of the TGA curve, at 88 °C, while for the Mt sample, the inflection point related to the evaporation of absorbed water appears at 94 °C. On further heating until 590 °C, the nil derivative values indicated that the samples have high purity. Clay decomposition, resulting from loss of hydroxyl units, is observed above 600 °C (note a small inflection in the dTGA

https://doi.org/10.1021/acs.jpcc.1c04322
J. Phys. Chem. C XXXX, XXX, XXX−XXX

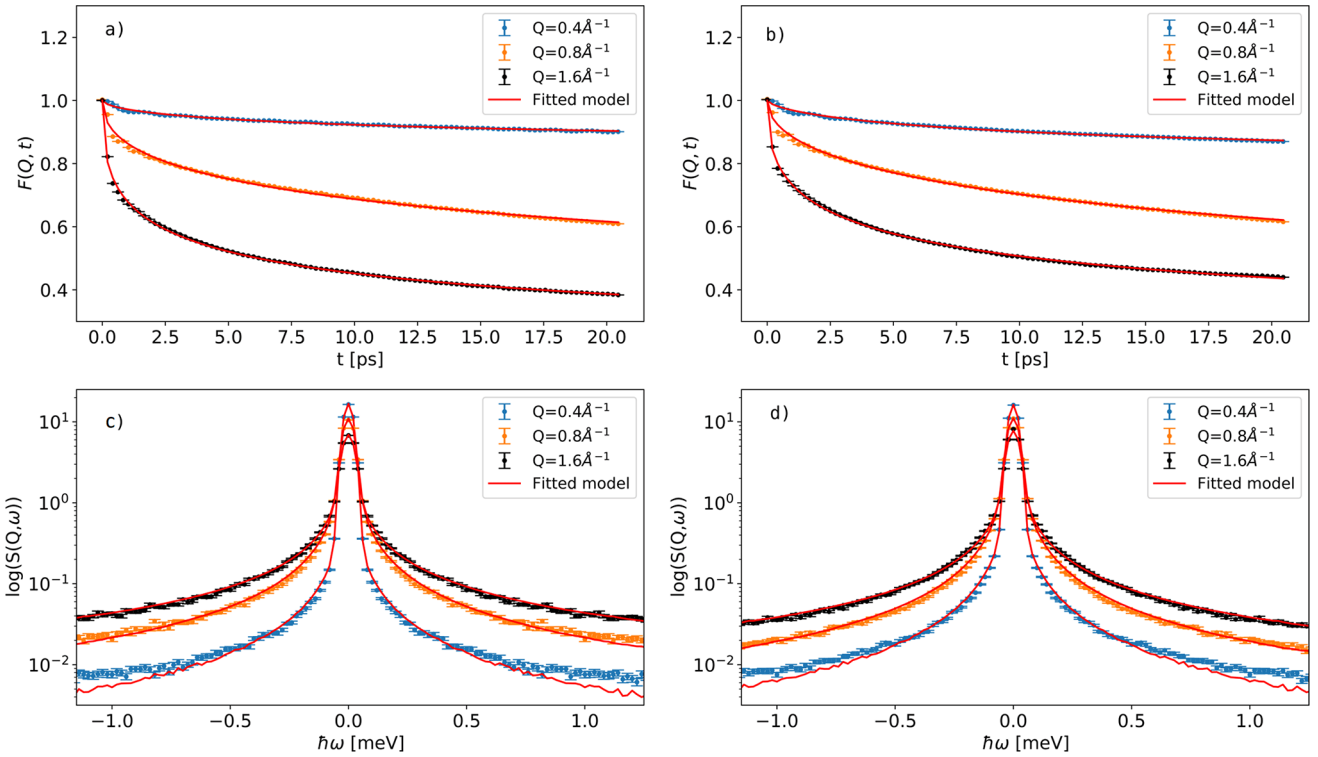

Figure 3. Symmetrized, normalized, and deconvolved $F(Q, t)$ data and fit result for (a) Ht and (b) Mt at 300 K. Fitted model transformed into the symmetrized, normalized, and convolved $S(Q, \omega)$ plotted with the experimental spectra of (c) Ht and (d) Mt at 300 K. A point to notice in Figure 3(c,d) is that for both samples, the fitted model follows the spectra best for high Q-values. The reason for this behavior is 3-fold. (i) Due to the low water content of the samples, we can expect water to be present largely only in the interlayer[8] and stronger interaction between the water and the clay surfaces and cations is foreseen. (ii) For low Q-values, contributions originating from the water molecule populations that coexist in the interlayer contribute to the dynamics observed. (iii) The opposite happens for high Q-values, where short-range motions with only few relaxations dominate.

curves, Figure 2(a)). Furthermore, based on these data, the number of water molecules in each sample was calculated, and it could be concluded that under the conditions for this study, both samples had around 3.5 H_2O per cation. This implied that the observed differences were attributed solely to the layer charge and the resulting exchangeable cation content of the interlayer. Furthermore, it is important to emphasize that at this relatively low water content long-range diffusion is essentially absent within the time window probed using AMATERAS. This is an important consideration for better understanding the QENS analysis discussed below.

Results obtained using the proposed model follow the data quite well as depicted in Figure 3(a,b). This assertion is further corroborated by Figure 3 (c,d), where the fitted model $F(Q, t)_{fit}$ for Ht and Mt is transformed into $S(Q, \omega)_{fit}$ (full lines) and compared with the measured spectra (markers). The reduced χ^2 for $S(Q, \omega)$ varies between 0.8 and 4.81, is reported in the Supporting Information, and is in good agreement with values reported for QENS data analysis using the analytical approach.[34,35] Additionally, it is well accepted that the maximum likelihood estimation based on the Poisson statistic is an excellent evaluation method to estimate parameters when analyzing counting experiments, particularly for small total numbers of counts.[36] Thus, we can infer that the proposed set of parameters is reliable.

The resulting parameters following this fit procedure at the different Q-values are presented in Figure 4. Notably, and as clearly observed in the inserted plot in Figure 4(b), for Q = 0.4 Å^{-1}, the proposed model captures the slight difference observed in the spectra of Mt and Ht. However, before we analyze in detail the results presented in Figure 4, it is important to recall that in clay minerals different populations of water molecules, classified according to their characteristic dynamics, coexist in the interlayer.[8,14,15] With this in mind, we can argue that the evolution of $\alpha(Q)$ vs Q corroborates the assumption that long-range processes are strongly coupled to local structural rearrangements (or structural relaxation),[8,17] where the presence of restricted diffusion is accounted for the observation that as $Q \rightarrow 0$, $\alpha < 1$ as depicted in Figure 4(a).[8,18] Of more interest is the consistent difference between $\alpha(Q)$ for Ht and Mt, suggesting different hydrogen relaxation processes in the two clay minerals. This is better understood by the analysis of the EISF, Figure 4(b), where we again observe almost the same Q-dependence for both samples, with slightly different magnitudes. Once more, the dependence of EISF(Q) on Q can be qualitatively interpreted based on the type of water population (motion) being probed. At low Q-values, the contribution originating from interlayer water is quite small, leading to a large EISF(Q). On the other hand, for higher Q-values, the dominant rotational relaxation gives rise to a larger QE contribution and consequently a decrease of EISF(Q).[8] Moreover, the slightly smaller EISF(Q) observed for Mt at lower Q-values confirmed that the average motional amplitudes of the interlayer water molecules (hydrogen atoms) were moderately larger when compared to Ht. Furthermore, in Figure 4(c) we observed that $\tau(Q)$ also showed similar Q-dependence with different magnitudes between 0.8 Å^{-1} $\leq Q \leq$ 1.2 A^{-1}. This difference is yet another

https://doi.org/10.1021/acs.jpcc.1c04322
J. Phys. Chem. C XXXX, XXX, XXX−XXX

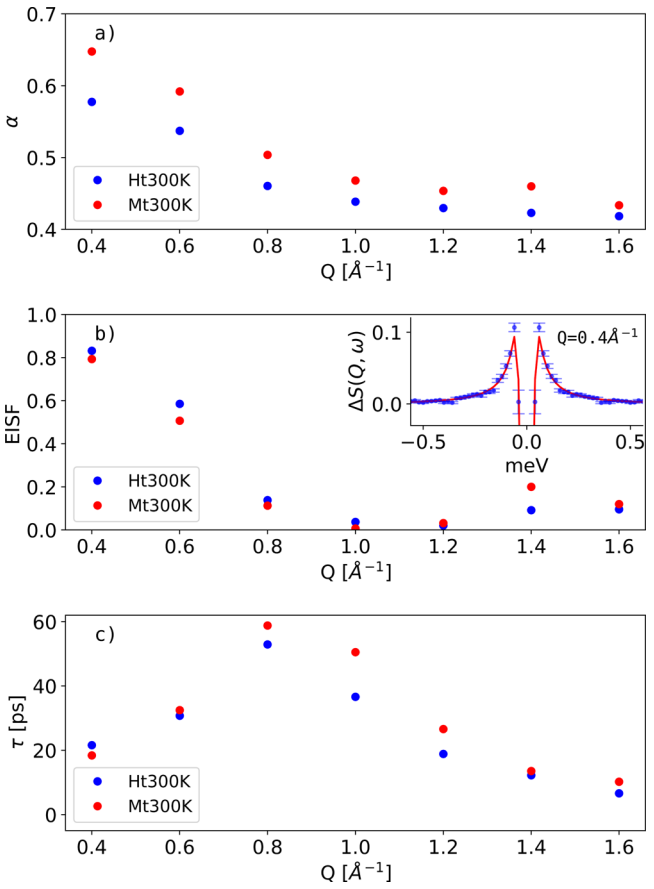

Figure 4. Water dynamics parameters for Mt and Ht at 300 K obtained using the model to fit $F(Q, t)$ described in the text. (a) α(Q), (b) the EISF(Q), together with a subplot of the difference in the spectra (the blue dots) and fitted models (the red line) between Mt and Ht at Q = 0.4 Å^{-1}, and (c) τ(**Q**). One point to make is that Mt and Ht have a Bragg reflection around Q = 1.4 Å^{-1}, explaining the larger EISF(Q).

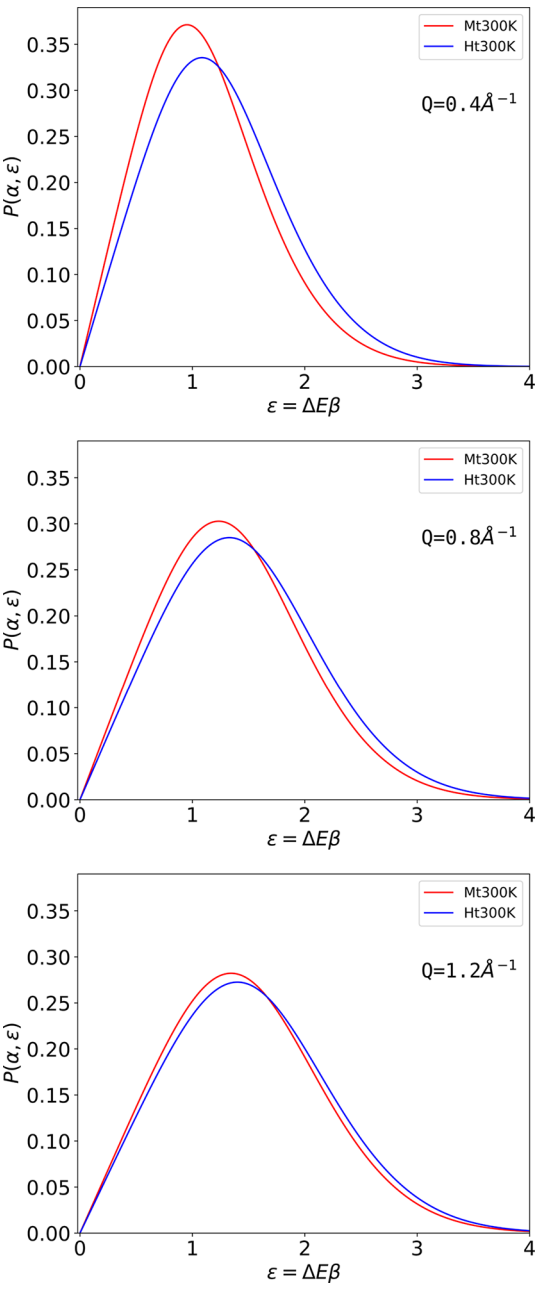

Figure 5. Distribution of the dimensionless energy barriers for three different Q-values at 300 K for both Mt and Ht using eq 17.

indication of subtle but distinct hydrogen relaxation processes in these minerals because for more localized motions, Mt relaxation is faster than for Ht.

Now we turn to the energy landscape interpretation, described by $P(\alpha, \varepsilon)$, Figure 5. As Q increased, the curves became equally broader, indicating that coupled long- and short-range motions lead to a non-Markovian diffusion process as previously observed in natrolite using NMR.[37] On the other hand, at low Q values, similarly to observations for human acetylcholinesterase with and without inhibitor,[19,20] the lower energy energy barrier and narrower distributions observed for Mt can be related to the reduced EISF, higher dehydration temperature, but lower enthaply, i.e., this barrier behavior reflects that more electrons are shared elsewhere and not in the water molecule. This can be explained by Mt polarizing the water molecules more in the interlayer than Ht, by making the ensemble of water molecules in the interlayer space less capable of hopping between the interlayer cation and the surface of its interlayer, hence not only distorting the water molecule tetragonal symmetry but also holding it longer.[14,15] This dynamical difference is fully corroborated by the thermal analysis results, Figure 2.

Finally, the evolution of the obtained parameters as a function of temperature and Q-values is presented for both Ht and Mt in Figure 6. In Figure 6(a) we observe that for both samples, with the exception of the lowest Q-value, α(Q) decreases on cooling, meaning that the form of the hydrogen relaxation becomes less exponential. From this figure, it is also clear that the evolution of α(Q) shows a change in behavior for Mt around 230 K and for Ht around 200 K, where the magnitude of α(Q) decreases more rapidly. This is related to the fact that the properties of the water molecules in the interlayer of the clays are not only distinct from those of bulk water (due to confinement) but also strongly affected by differences in expression of the surface charges (polarization effect) between Mt and Ht.

Similarly to the evolution of the experimental EISF(Q) vs T previously reported for Mt,[8] the obtained EISF(Q) parameter, Figure 6(b), increases as the temperature decreases, this behavior being more noticeable for higher Q-values. Additionally, changes in its evolution are noticeable at 270 K for both

https://doi.org/10.1021/acs.jpcc.1c04322
J. Phys. Chem. C XXXX, XXX, XXX−XXX

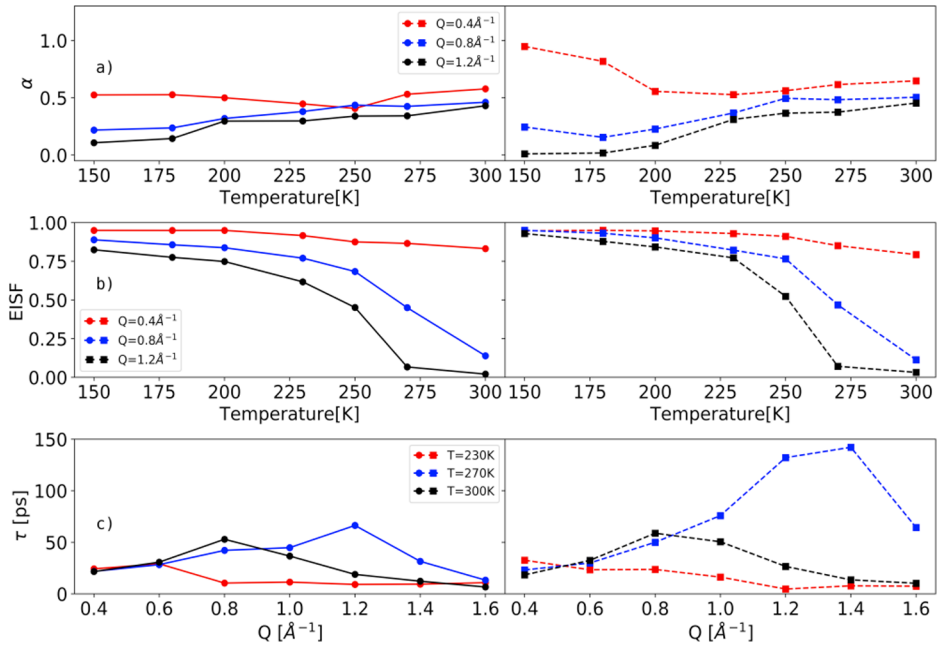

Figure 6. Water dynamics parameters for Ht (left, circles and line) and Mt (right, squares and dotted line) at different temperatures obtained using the model to fit $F(Q, t)$ described in the text. (a) $\alpha(Q)$, (b) the EISF(Q), and (c) $\tau(Q)$ at three different temperatures as a function of Q.

samples, at 230 K for Mt, and at 200 K for Ht. This observation is yet another indication that dynamical transitions occurring in the samples are related to a damping of the average motional amplitude of the hydrogen relaxation. Of more interest is the fact that below 270 K the EISF(Q) for Mt is consistently larger than for Ht at all Q-values implying that its greater layer charge induces stronger hydrogen bonds, leading to smaller average motional amplitude and faster crystallization. This is in full agreement with the idea that the properties of interlayer water molecules are highly influenced by the clay surfaces being more liquid-like at low surface charges (Ht) and becoming more ice-like at high surface charges (Mt).[38]

In Figure 6(c) we observe that the evolution of $\tau(Q)$ shows that the model captures different dynamics originating from the activation of different amounts and populations of water molecules.[13] In general the behavior is not very different between the two clay minerals. However, $\tau(Q)$ for Mt at 270 K shows a clear increase in the magnitude as Q increases. This observation, together with the reduced value of the EISF(Q), fully corroborated the energy landscape interpretation, i.e., a mixture of different fractions of water coexist in the interlayer and the surface charge dominates the freezing behavior.

CONCLUSION

With this new approach to analyzing QENS data, we reproduced the experimental data quite well, showing how adequately the minimal model approach can capture relaxation dynamics of the water molecules confined in these 2D-layered systems. Two scenarios can be evoked for the physical interpretation of multiscale relaxation leading to Mittag–Leffler relaxation function: continuous time random walks, i.e., by diffusion with trapping and a broad distribution of residence times as proposed by Scher and Montroll,[39] or by diffusion with long-time memory kernels, which can be related to the general Langevin equation.[26,40] Both descriptions support the concept that the process of water diffusion in clay minerals is a cooperative process, in which the layer surface charge, the exchangeable cation, and the water molecules participate. On the basis of this interpretation, we obtained direct information on the polarization effect on the water molecules by the interlayer charge in two distinct clay minerals, where the greater residual surface electron density in Mt induces larger distortion of the water tetragonal symmetry and slower diffusion when compared to Ht at 300 K. This knowledge is extremely relevant and crucial for understanding the role of exchangeable cations in many industrial applications of clay systems. However, this information can neither be easily obtained from experimental data nor fully described using molecular dynamics simulations.

Additionally, a better understanding of the freezing behavior of water in these nanomaterials was proposed. On the basis of our analysis for the QENS data obtained at different temperatures, we showed that due to the polarization of the water molecules induced by higher surface charge the freezing temperature of supercooled water is higher in Mt. These results are of special interest in environmental research because the significant portion of the water that remains unfrozen in a liquid or semiliquid state in soils plays an important role in frost heaving, shock wave transmission, and radioactive waste disposal among others.

To conclude, the newly introduced minimalistic model for $F(Q, t)$ is quite robust, simple to use with only three fitting parameters, and gives crucial information about the dynamics of the water molecules responsible for many properties of clay minerals, such as complexation of radioactive waste or delivery of bioactive molecules. There is therefore a big potential for applying this simple theoretical model in the study of confined water. Indeed, in the future this approach for analyzing QENS data is expected to become a new common analysis method for investigating incoherent QE dynamics of atoms. For further work, other statistical methods to estimate the uncertainties for the $F(Q, t)$, through the Fourier transformation, should be investigated.

https://doi.org/10.1021/acs.jpcc.1c04322
J. Phys. Chem. C XXXX, XXX, XXX−XXX

■ ASSOCIATED CONTENT

Supporting Information

The Supporting Information is available free of charge at https://pubs.acs.org/doi/10.1021/acs.jpcc.1c04322.

Raw experimental quasi-elastic neutron scattering (QENS) data and goodness of the fit for the 2D-layered clay minerals montmorillonite (Mt) and hectorite (Ht) (PDF)

■ AUTHOR INFORMATION

Corresponding Authors

Gerald Kneller − *Centre de Biophysique Moléculaire, CNRS and Université d'Orléans, 45071 Orléans, France; Synchrotron Soleil; L'Orme de Merisiers, 91192 Gif-sur-Yvette, France*; Email: gerald.kneller@cnrs.fr

Heloisa N. Bordallo − *Niels Bohr Institute, University of Copenhagen, Copenhagen 2100, Denmark; Institute for Frontier Materials, Deakin University, Burwood, VIC, Australia; European Spallation Source (ESS), Lund, Sweden;* orcid.org/0000-0003-0750-0553; Email: bordallo@nbi.ku.dk

Authors

Martin H. Petersen − *Niels Bohr Institute, University of Copenhagen, Copenhagen 2100, Denmark*

Nathan Vernet − *Niels Bohr Institute, University of Copenhagen, Copenhagen 2100, Denmark*

Will P. Gates − *Institute for Frontier Materials, Deakin University, Burwood, VIC, Australia;* orcid.org/0000-0001-7388-0289

Félix J. Villacorta − *Consorcio ESS-Bilbao. Parque Científico y Tecnológico, 48170 Zamudio, Spain;* orcid.org/0000-0001-7257-9208

Seiko Ohira-Kawamura − *Materials and Life Science Division, J-PARC Center, Tokai, Ibaraki 319-1195, Japan*

Yukinobu Kawakita − *Materials and Life Science Division, J-PARC Center, Tokai, Ibaraki 319-1195, Japan*

Masatoshi Arai − *European Spallation Source (ESS), Lund, Sweden*

Complete contact information is available at: https://pubs.acs.org/10.1021/acs.jpcc.1c04322

Notes

The authors declare no competing financial interest.

■ ACKNOWLEDGMENTS

This project was funded the Danish Agency for Science, Technology and Innovation through DANSCATT. The neutron scattering experiment at J-PARC was performed under the J-PARC Long-Term Proposal (proposal no. 2018L1000). The thermal analysis apparatus were financed by the Carlsbergfond grant ref: 2013-01-0589.

■ REFERENCES

(1) Dashtian, H.; Wang, H.; Sahimi, M. Nucleation of Salt Crystals in Clay Minerals: Molecular Dynamics Simulation. *J. Phys. Chem. Lett.* **2017**, *8*, 3166−3172.

(2) Gimmi, T.; Churakov, S. V. Water retention and diffusion in unsaturated clays: Connecting atomistic and pore scale simulations. *Appl. Clay Sci.* **2019**, *175*, 169−183.

(3) Carignani, E.; Borsacchi, S.; Blasi, P.; Schoubben, A.; Geppi, M. Dynamics of Clay-Intercalated Ibuprofen Studied by Solid State Nuclear Magnetic Resonance. *Mol. Pharmaceutics* **2019**, *16*, 2569−2578.

(4) Thiebault, T.; Boussafir, M.; Le Forestier, L.; Le Milbeau, C.; Monnin, L.; Guégan, R. Competitive adsorption of a pool of pharmaceuticals onto a raw clay mineral. *RSC Adv.* **2016**, *6*, 65257−65265.

(5) Thiebault, T.; Brendle, J.; Auge, G.; Limousy, L. Zwitterionic-surfactant modified LAPONITE for removal of ions (Cs^+ Sr^{2+} and Co^{2+}) from aqueous solutions as a sustainable recovery method for radionuclides from aqueous wastes. *Green Chem.* **2019**, *21*, 5118−5127.

(6) Hunvik, K. W. B.; Loch, P.; Cavalcanti, L. P.; Seljelid, K. K.; Roren, P. M.; Rudic, S.; Wallacher, D.; Kirch, A.; Knudsen, K. D.; Rodrigues Miranda, C.; et al. CO_2 Capture by Nickel Hydroxide Interstratified in the Nanolayered Space of a Synthetic Clay Mineral. *J. Phys. Chem. C* **2020**, *124*, 26222−26231.

(7) Ehlmann, B. L.; Mustard, J. F.; Murchie, S. L.; Bibring, J.-P.; Meunier, A.; Fraeman, A. A.; Langevin, Y. Subsurface water and clay mineral formation during the early history of Mars. *Nature* **2011**, *479*, 53−60.

(8) Bordallo, H. N.; Aldridge, L. P.; Churchman, G. J.; Gates, W. P.; Telling, M. T. F.; Kiefer, K.; Fouquet, P.; Seydel, T.; Kimber, S. A. J. Quasi-Elastic Neutron Scattering Studies on Clay Interlayer-Space Highlighting the Effect of the Cation in Confined Water Dynamics. *J. Phys. Chem. C* **2008**, *112*, 13982−13991.

(9) Delage, P.; Cui, Y.; Tang, A. Clays in radioactive waste disposal. *Journal of Rock Mechanics and Geotechnical Engineering* **2010**, *2*, 111−123.

(10) Tesson, S.; Louisfrema, W.; Salanne, M.; Boutin, A.; Ferrage, E.; Rotenberg, B.; Marry, V. Classical Polarizable Force Field To Study Hydrated Charged Clays and Zeolites. *J. Phys. Chem. C* **2018**, *122*, 24690−24704.

(11) Hånde, R.; Ramothe, V.; Tesson, S.; Dazas, B.; Ferrage, E.; Lanson, B.; Salanne, M.; Rotenberg, B.; Marry, V. Classical Polarizable Force Field to Study Hydrated Hectorite: Optimization on DFT Calculations and Validation against XRD Data. *Minerals* **2018**, *8*, 205.

(12) Marty, N. C. M.; Grangeon, S.; Lassin, A.; Madé, B.; Blanc, P.; Lanson, B. A quantitative and mechanistic model for the coupling between chemistry and clay hydration. *Geochim. Cosmochim. Acta* **2020**, *283*, 124−135.

(13) Gates, W. P.; Seydel, T.; Bordallo, H. N. Layer charge effects on anisotropy of interlayer water and structural OH dynamics in clay minerals probed by high-resolution neutron spectroscopy. *Appl. Clay Sci.* **2021**, *201*, 105928.

(14) Ignazzi, R.; Gates, W. P.; Diallo, S. O.; Yu, D.; Juranyi, F.; Natali, F.; Bordallo, H. N. Electric Field Induced Polarization Effects Measured by in Situ Neutron Spectroscopy. *J. Phys. Chem. C* **2017**, *121*, 23582−23591.

(15) Gates, W. P.; Bordallo, H. N.; Aldridge, L. P.; Seydel, T.; Jacobsen, H.; Marry, V.; Churchman, G. J. Neutron Time-of-Flight Quantification of Water Desorption Isotherms of Montmorillonite. *J. Phys. Chem. C* **2012**, *116*, 5558−5570.

(16) Skipper, N. T.; Lock, P. A.; Titiloye, J. O.; Swenson, J.; Mirza, Z. A.; Howells, W. S.; Fernandez-Alonso, F. The structure and dynamics of 2-dimensional fluids in swelling clays. *Chem. Geol.* **2006**, *230*, 182−196.

(17) Chen, S. H.; Liao, C.; Sciortino, F.; Gallo, P.; Tartaglia, P. Model for single-particle dynamics in supercooled water. *Phys. Rev. E: Stat. Phys., Plasmas, Fluids, Relat. Interdiscip. Top.* **1999**, *59*, 6708.

(18) Zanotti, J.-M.; Bellissent-Funel, M.-C.; Chen, S.-H. Relaxational dynamics of supercooled water in porous glass. *Phys. Rev. E: Stat. Phys., Plasmas, Fluids, Relat. Interdiscip. Top.* **1999**, *59*, 3084−3093.

(19) Saouessi, M.; Peters, J.; Kneller, G. R. Asymptotic analysis of quasielastic neutron scattering data from human acetylcholinesterase reveals subtle dynamical changes upon ligand binding. *J. Chem. Phys.* **2019**, *150*, 161104.

(20) Saouessi, M.; Peters, J.; Kneller, G. R. Frequency domain modeling of quasielastic neutron scattering from hydrated protein

powders: Application to free and inhibited human acetylcholinesterase. *J. Chem. Phys.* **2019**, *151*, 125103.
(21) Kneller, G. Franck−Condon picture of incoherent neutron scattering. *Proc. Natl. Acad. Sci. U. S. A.* **2018**, *115*, 9450.
(22) Condon, E. A theory of intensity distribution in band systems. *Phys. Rev.* **1926**, *28*, 1182−1201.
(23) Lovensy, S. W. *Theory of Neutron Scattering from Condensed Matter*; Oxford University Press: Oxford, 1984.
(24) Schofield, P. Space-Time correlation function formalism for slow neutron scattering. *Phys. Rev. Lett.* **1960**, *4*, 239.
(25) Gorenflo, R.; Kilbas, A. A.; Mainardi, F.; Rogosin, S. V. *Mittag-Leffler Functions, Related Topics and Applications*; Spinger Monographs in Mathematics; Springer: Heidelberg, 2014.
(26) Metzler, R.; Jeon, J.-H.; Cherstvy, A. G.; Barkai, E. Anomalous diffusion models and their properties: non-stationarity, non-ergodicity, and ageing at the centenary of single particle tracking. *Phys. Chem. Chem. Phys.* **2014**, *16*, 24128−24164.
(27) Nakajima, K.; Ohira-Kawamura, S.; Kikuchi, T.; Nakamura, M.; Kajimoto, R.; Inamura, Y.; Takahashi, N.; Aizawa, K.; Suzuya, K.; Shibata, K.; et al. AMATERAS: A Cold-Neutron Disk Chopper Spectrometer. *J. Phys. Soc. Jpn.* **2011**, *80*, SB028.
(28) Inamura, Y.; Nakatani, T.; Suzuki, J.; Otomo, T. Development Status of Software Utsusemi, for Chopper Spectrometers at MLF, J-PARC. *J. Phys. Soc. Jpn.* **2013**, *82*, SA031.
(29) Berrod, Q.; Lagrené, K.; Zanotti, J.-M.; Ollivier, J. Inelastic and quasi-elastic neutron scattering. Application to soft-matter. *EPJ Web Conf.* **2018**, *188*, 05001.
(30) Toby, B. H.; Egami, T. Accuracy of pair distribution function analysis applied to crystalline and non-crystalline materials. *Acta Crystallogr., Sect. A: Found. Crystallogr.* **1992**, *48*, 336−346.
(31) Ravel, B. *Quantitative EXAFS Analysis*; online (accessed April 22, 2021); John Wiley and Sons, Ltd: Chichester, 2014.
(32) Azuah, R. T.; Kneller, L. R.; et al. DAVE: A Comprehensive Software Suite for the Reduction, Visualization, and Analysis of Low Energy Neutron Spectroscopic Data. *J. Res. Natl. Inst. Stand. Technol.* **2009**, *114*, 341−358.
(33) Dembinski, H.; Ongmongkolkul, P.; Deil, C.; Hurtado, D. M.; Schreiner, H.; Feickert, M.; Andrew; Burr, C.; Rost, F.; Pearce, A.; et al. *scikit-hep/iminuit*, 2020; DOI: 10.5281/zenodo.4310361.
(34) Martins, M.; Dinitzen, A.; Mamontov, E.; Rudic, S.; Pereira, J.; Hartmann-Petersen, R.; Herwig, K.; Bordallo, H. Water dynamics in MCF-7 breast cancer cells: a neutron scattering descriptive study. *Sci. Rep.* **2019**, *9*, 8704.
(35) Stavretis, S. E.; Mamontov, E.; Moseley, D. H.; Cheng, Y.; Daemen, L. L.; Ramirez-Cuesta, A. J.; Xue, Z.-L. Effect of magnetic fields on the methyl rotation in a paramagnetic cobalt(II) complex. Quasielastic neutron scattering studies. *Phys. Chem. Chem. Phys.* **2018**, *20*, 21119−21126.
(36) Hauschild, T.; Jentschel, M. Comparison of maximum likelihood estimation and chi-square statistics applied to counting experiments. *Nucl. Instrum. Methods Phys. Res., Sect. A* **2001**, *457*, 384−401.
(37) Sapiga, A.; Sergeev, N. NMR study of microscopic mechanism of water molecules diffusion in natrolite. *Solid State Nucl. Magn. Reson.* **2019**, *97*, 1−6.
(38) Li, Q.; Li, X.; Yang, S.; Gu, P.; Yang, G. Structure, Dynamics, and Stability of Water Molecules during Interfacial Interaction with Clay Minerals: Strong Dependence on Surface Charges. *ACS Omega* **2019**, *4*, 5932−5936.
(39) Scher, H.; Montroll, E. W. Anomalous transit-time dispersion in amorphous solids. *Phys. Rev. E* **1975**, *12*, 2455−2477.
(40) Kneller, G. R. Generalized Kubo relations and conditions for anomalous diffusion: Physical insights from a mathematical theorem. *J. Chem. Phys.* **2011**, *134*, 224106.

https://doi.org/10.1021/acs.jpcc.1c04322
J. Phys. Chem. C XXXX, XXX, XXX−XXX